ELSEVIER

PSYCHIATRY
RESEARCH
NEUROIMAGING

Psychiatry Research: Neuroimaging Section 91 (1999) 11–30 www.elsevier.com/locate/psychresns

Automated Talairach atlas-based parcellation and measurement of cerebral lobes in children

Wendy R. Kates[a,b], Ilana S. Warsofsky[c], Anil Patwardhan[c], Michael T. Abrams[a,b], Alex M.C. Liu[c], SakkuBai Naidu[a,d,e], Walter E. Kaufmann[a,b,d,e,f], Allan L. Reiss[c,g,*]

[a] *The Kennedy Krieger Institute, 707 N. Broadway, Baltimore, MD 21205, USA*
[b] *Department of Psychiatry, Johns Hopkins University of School of Medicine, Baltimore, MD, USA*
[c] *Divison of Child and Adolescent Psychiatry and Child Development, Department of Psychiatry, Stanford University School of Medicine, 401 Quarry Road, Stanford, CA 94305–5719, USA*
[d] *Department of Neurology, Johns Hopkins University of School of Medicine, Baltimore, MD, USA*
[e] *Department of Pediatrics, Johns Hopkins University School of Medicine, Baltimore, MD, USA*
[f] *Department of Pathology, Johns Hopkins University School of Medicine, Baltimore, MD, USA*
[g] *Department of Pediatrics, Stanford University School of Medicine, Stanford, CA 94305-5719, USA*

Received 13 October 1998; received in revised form 5 March 1999; accepted 17 March 1999

Abstract

This study applied a Talairach-based automated parcellation method, originally proposed for adults, to the measurement of lobar brain regions in pediatric study groups. Manual measures of lobar brain regions in a sample of 15 healthy boys, girls and adults were used initially to revise the original Talairach-based grid to increase its applicability to pediatric brains. The applicability of the revised Talairach grid was then tested on an independent sample of five girls with Rett syndrome. As Tables 3 and 4 in the text demonstrate, sensitivity, specificity and positive predictive values either remained unchanged or increased as a result of revising the sectors to fit the brains of children. High levels of sensitivity and specificity were achieved for all revised Talairach-based calculations in relation to the manual measures. Both positive predictive values and intraclass correlations between volumetric measures produced by the revised automated and manual methods varied with the relative size of the brain region. Values were relatively low for smaller structures such as the brainstem and subcortical region, and high for lobar regions. These results suggest that the automated Talairach atlas-based parcellation method can produce sensitive

* Corresponding author. Tel.: +1-650-498-4538; fax: +1-650-723-5531.
E-mail address: areiss1@leland.stanford.edu (A.L. Reiss)

PII: S0925-4927(99)00011-6

and specific volumetric measures of lobar brain regions in both normal children and children with brain disorders. Accordingly, the method holds much promise for facilitating quantitative pediatric neuroimaging research.

Keywords: Brain parcellation; Pediatric; Sensitivity; Specificity; Positive predictive value

1. Introduction

The refinement of structural neuroimaging methods during the past decade has significantly advanced our understanding of brain development in both healthy children and those with specific neurological and psychiatric disorders. An important goal in many imaging studies is to parcellate, or divide the brain into neurofunctional regions, measure and compare the volumes of those regions in specific pediatric study groups, and analyze structural–functional relations that may be associated with those brain regions. A prominent method for achieving this goal consists of manually tracing the region of interest (ROI) on each image in which the ROI appears in a 'stack' of images comprising a three-dimensional (3D) dataset. However, manual tracing is labor-intensive, and the development of standard, reliable and valid manual measurement protocols is time consuming. This often restricts the application of this method to small samples, limiting the power and generalizability of the results.

Researchers in adult neuroimaging have attempted to address this issue by developing automated parcellation methods that permit the rapid and standardized measurement of neurofunctional regions of interest in MRI datasets. Andreasen et al. (1994, 1996) utilized the stereotaxic coordinate system described by Talairach and Tournoux (1988) to develop a computer software module that positionally normalizes the brain and maps a three-dimensional proportional grid onto it. This grid consists of 1232 three-dimensional rectangular sectors that can be grouped together into neurofunctional regions of interest. Andreasen and colleagues compared this method of parcellation to manual methods using sulcal, gyral and in-plane neuroanatomical boundaries, and demonstrated that their automated parcellation method could be used to measure lobar brain regions in adults in a reliable manner. In addition, Andreasen and colleagues provided preliminary validation of the method by demonstrating convergence between automated measures and manually based measures in schizophrenic patients.

In the present study, the Talairach-based automated parcellation method is applied to the measurement of children's brains to determine whether this technique can be used in a reliable and valid manner with pediatric study groups. In the initial phase of this study (Kaplan et al., 1997), we revised the computerized grid originally proposed by Andreasen and coworkers, and demonstrated the reliability and validity of this method for measuring major brain regions such as the cerebrum and the cerebellum. In the present study, a sample of healthy boys, girls and adults was used to revise the Talairach sectors further, in order to parcellate and measure the four cerebral lobes, and to increase the method's applicability to pediatric study groups. The applicability of the revised Talairach definitions was then tested on an independent sample of girls with Rett syndrome, a severe developmental disorder known to be associated with global microcephaly and specific morphological changes in the frontal lobe and the subcortical regions of the brain (Subramaniam et al., 1997a). Sensitivity, specificity and positive predictive values based on the original Talairach grid developed by Andreasen and colleagues were compared to values based on our revised Talairach grid, in order to determine if the revised Talairach atlas fit pediatric brain morphology more accurately. Accordingly, the results reported here reflect an important step in determining whether the successful application of this automated atlas-based parcel-

lation method to children has the potential to enhance the acquisition of much needed knowledge relating to normal and abnormal brain development in children.

2. Methods

2.1. Subjects

Scans from 15 healthy individuals and five individuals with Rett syndrome were obtained from participants in ongoing studies of brain development in normal individuals and in those with genetic and developmental disorders. The 15 healthy individuals had no history of psychiatric, neurological, or learning problems. They consisted of five normal girls (mean age = 9.12.; S.D. = 2.7), five normal boys (mean age = 8.49; S.D. = 1.50), and five normal adults (three males, two females; mean age = 34.98; S.D. = 6.97). Adults were included in order to ensure the breadth of applicability of the revised method to both children and adults. The five girls with Rett syndrome, individually matched by age to the five normal girls, had a mean age of 8.06, with an S.D. of 0.707. IQ scores were obtained with standardized psychometric instruments (Thorndike et al., 1986; Wechsler, 1991) on the normal girls (mean IQ = 87; S.D. = 5.3) and the normal boys (mean IQ = 120, S.D. = 7.6). (The discrepancy between the IQ scores of the boys and girls most likely was related to differences in ascertainment methods for the respective studies in which they participated; accordingly, this discrepancy may affect the comparability of the findings between each gender.) IQ scores were available on only three of the adults (mean IQ = 112; S.D. = 29) and none of the girls with Rett syndrome (due to their profound and pervasive developmental delays).

2.2. Image acquisition and processing

MRI images of each subject's brain were acquired with a GE-Signa 1.5 T scanner (General Electric, Milwaukee, WI, USA). Coronal T1 weighted images were acquired with a 3D volumetric radiofrequency spoiled gradient echo (SPGR) series with the following scan parameters: TR = 35–45, TE = 5–7, flip angle = 45, NEX = 1, matrix size = 256 × 128, field of view = 20–24. This SPGR series was partitioned into 124, 1.5-mm contiguous slices. Raw GE-Signa formatted image data were transferred from the MRI scanner to Macintosh workstations via existing network connections. The image data were imported into the program *BrainImage* (Reiss, 1998) for visualization, processing, and analysis (Subramaniam et al., 1997b). The importation process converts the dataset into eight-bit images, and corrects for shading artifacts due to signal inhomogeneity between slices. Non-brain material (e.g. skull, scalp, and vasculature) is removed from these image stacks using a semi-automated edge detection process that involves a region growing/dilation routine. These 'skull stripped' images are resliced, making the interpolated slice thickness corresponding to the z-dimension the same as the x and y pixel dimensions, thereby converting the image stacks into cubic voxel datasets. The cubic voxel datasets are opened into the multiplanar visualization module of *BrainImage* so that three orthogonal representations of the data can be viewed simultaneously. Within the multiplanar module, new datasets in the coronal and axial orientations are created to standardize positional normalization across all subjects, and to optimize drawing of gold standard regions within the cerebrum and posterior fossa, respectively.

2.3. Manual delineation of 'gold standard' regions of interest

For this study, the boundaries of the frontal, parietal, occipital and temporal lobes, subcortical region, brainstem and cerebellum were manually delineated and the volumes measured. Prior to the measurement of these structures, cerebrospinal fluid (CSF) was removed from the dataset, using a semi-automated segmentation technique (Otsu, 1979) to identify all voxels with CSF-like intensity. The manually derived measurements of each region constituted the 'gold

standard' to which the measure of each Talairach-defined region was compared. The rules that were used to delineate each structure were based on the rules described by Andreasen et al. (1996). When necessary, modifications were developed in our laboratory in consultation with an experienced pediatric neuroanatomist (W.E.K.), who also reviewed all manually drawn ROIs prior to measurement. The rules used to delineate each region are described in Appendix A.

2.4. Talairach-defined regions

The method described by Andreasen et al. (1996) was used to delineate the Talairach-defined regions. A proportional stereotaxic grid is overlaid onto the brain following a linear transformation based on the rater's identification of three anchor points (the anterior commissure, the posterior commissure, and a midsagittal point above the axis created by the first two points), and the subsequent automated identification of the most anterior, posterior, right lateral, left lateral, superior and inferior points of the brain. The grid is composed of 1232 three-dimensional rectangular sectors (Andreasen et al., 1994, 1996) which are grouped together into regions corresponding to neuroanatomical structures of interest (Talairach and Tournoux, 1988). Andreasen and colleagues originally used adult brains to form the basis of their assignment of sectors to particular regions.

In order to create comparable Talairach-defined regions from pediatric subjects, as well as adults, the manual (gold standard) ROIs from each subject (e.g. girls, boys and adults) were used. First, each voxel within an individual brain was labeled as belonging to only one gold standard brain region (e.g. frontal lobe, temporal lobe, cerebellum, etc.) based on the manual parcellation described above. Next, the composition of labeled voxels that made up each of the 1232 Talairach sectors was determined for each subject. For each subject group, the Talairach sector was assigned to the Talairach brain region that was represented by the majority (or plurality) of the labeled voxels. If the sector assignment was consistent for all subject groups, that assignment was incorporated into our pediatric-based regional definition.

We found that for our pediatric sample, approximately one-quarter of the sectors did not correspond consistently (across groups) to the regions to which they were originally assigned by Andreasen and co-workers. (These sectors usually bordered two or three separate brain regions.) Data for these sectors were reviewed, and disagreements between our sector assignments and those proposed by Andreasen and colleagues were resolved using the following criteria: if the majority of our subject groups were consistent in sector assignment on both the left and right sides, and if that assignment was consistent with the neuroanatomic region originally proposed by Talairach and Tournoux, the sector was reassigned to that region. In ambiguous cases, the images were viewed and the sector was assigned to the region that was featured most prominently in the manually drawn ROI. If the sector was not assigned to any region based on our sample (i.e. the sector contained non-brain material or air), the sector was kept in the original region to which it had been assigned by Andreasen and colleagues (Fig. 1). The final list of sectors corresponding to each region of interest is provided in Appendix B.

Once all sector assignments were made, automated volume measurements of the Talairach-defined regions were carried out. Volume estimates were based on an algorithm that summed cubic voxels across all sectors assigned to a specific region and that converted those sums to cubic centimeter units. (Interested readers are invited to contact the author for additional information.) In order to ensure that measurements for all lobes, the brainstem and cerebellum were composed of gray and white tissue only, the measures were made on brain images in which non-ventricular CSF had been removed with an automated histogram-based threshold selection method (Otsu, 1979). A fuzzy tissue segmentation algorithm (Reiss et al., 1998) also was used to divide the voxels constituting brain tissue into gray matter and white matter. Only gray matter voxels were used in the assessment of the sensitivity,

specificity and positive predictive value of the subcortical region.

For the normal children and adults on which the revised sectors were based, manual measurements were compared only to measurements of revised Talairach-defined regions. For the girls with Rett syndrome, manual measurements were compared to measurements based on both the original and the revised Talairach-defined regions.

2.5. Data analysis

The following definitions of sensitivity, specificity and positive predictive values (PPV) of the Talairach-defined regions in relation to the gold standard regions were used: sensitivity was defined as the portion of the gold standard region correctly included within the Talairach region, specificity as the portion of the non-gold standard region correctly excluded from the Talairach re-

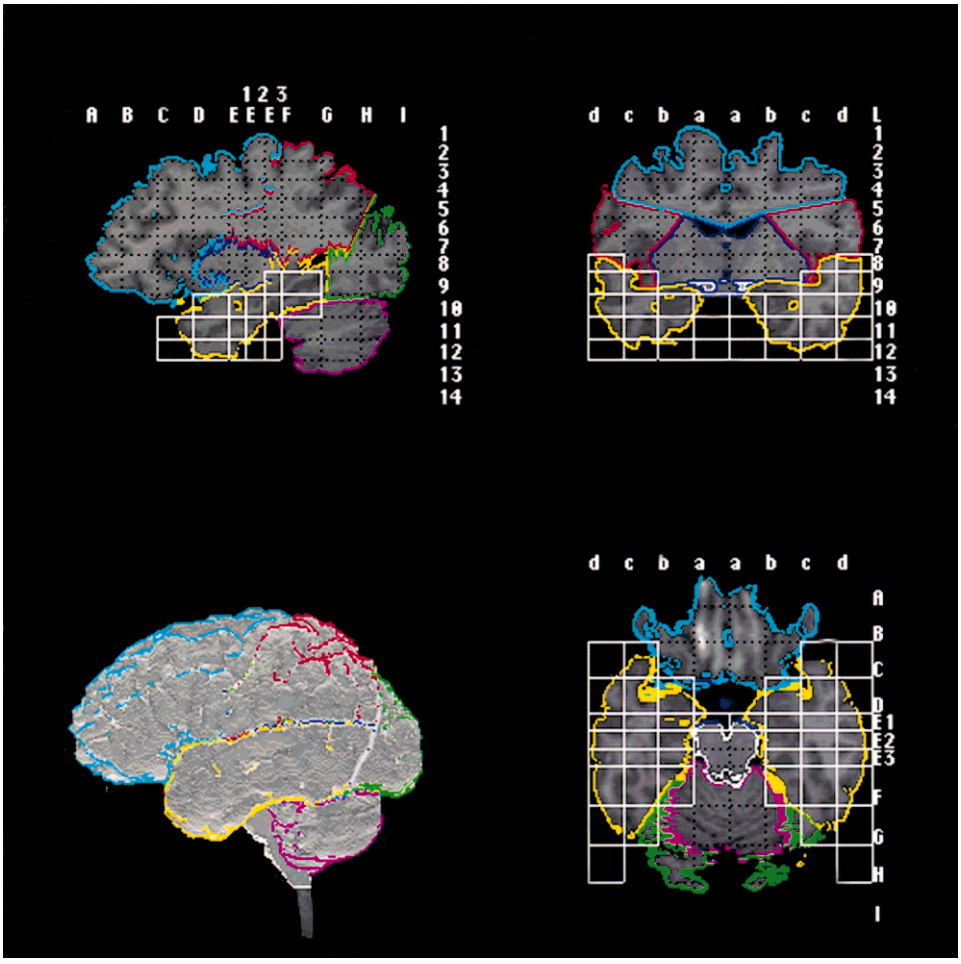

Fig. 1. The Talairach coordinate system appears to have sufficient sensitivity, specificity and usefulness for automatically localizing and measuring the major lobes of the brain as well as large regions such as the cerebellum and lateral ventricles. In this figure, the brain has been positionally normalized and Talairach sectors designated as representing the temporal lobe are shown superimposed over manually derived sulcal-based, 'gold-standard' regions. In this illustration, the gold-standard temporal lobe boundaries are designated in yellow and the Talairach sectors as white boxes in the three orthogonal views. In order to calculate temporal lobe volume, the voxels in all slices that are designated as temporal lobe are summed.

gion, and PPV as the portion of the Talairach region that overlapped with the gold standard region. For additional information, see Kaplan et al. (1997). Sensitivity, specificity and positive predictive values based on original Talairach sectors were compared to values based on revised Talairach sectors with the Wilcoxon Signed Rank Test. Pair-wise correspondence between gold standard regional volumes and Talairach-defined regional volumes was evaluated with both the Pearson R and the intraclass correlation coefficient (ICC). In order to assess whether findings based on the Talairach method converged with previously reported group differences based on manual measurements, gold standard and Talairach-defined regional volumes, corrected for whole brain volume, were compared between girls with Rett syndrome and age-matched normal girls, and between normal girls and normal boys. These comparisons were carried out with the Wilcoxon Signed Rank Test due to the non-normal distribution of the data. All statistical analyses presented in this report should be viewed as preliminary given the small size of the experimental group.

3. Results

3.1. Sector reassignment

A total of 121 (9.82%) sectors were reassigned from the atlas proposed by Andreasen and colleagues. The number of reassigned sectors per region ranged from 0 for the brainstem to 29 (2.35% of total brain sectors; 24% of total reassigned sectors) for the occipital lobe.

3.2. Sensitivity, specificity, positive predictive value, and correlations

Table 1 shows the sensitivity, specificity and positive predictive values for revised Talairach-based measurements of all regions of interest, and the intraclass and Pearson R correlations between Talairach-defined and gold standard measures. Because the measurements for the normal boys and girls did not vary by gender, the data are grouped by normal children ($n = 10$), normal adults ($n = 5$), and all normal subjects ($n = 15$). The measures shown for each group in Table 1 represent the mean values across all subjects. Since these subjects represent the sample from which the revised Talairach sectors were derived, this table is included to illustrate the potential strengths and weaknesses of the automated parcellation approach. The applicability of the method to an independent sample is illustrated below with data drawn from a sample of girls with Rett syndrome.

Sensitivity values were high overall, ranging from a mean of 0.79 to 0.95 for all regions. The values obtained were comparable to those reported for adults by Andreasen et al. (1996), which ranged from 0.81 to 0.93. Specificity values for all child and adult brains were uniformly high, ranging from a mean of 0.95 for the parietal region to 0.99 for the cerebellum. These values also were all comparable to the specificity values for adult brains reported by Andreasen and colleagues (which ranged from 0.98 to 0.99).

Positive predictive values ranged widely, from 0.60 for the brainstem to 0.95 for the frontal lobe. Values were consistent between child and adult study groups. Overall, variations in PPV were related to size of brain region: values were lower for smaller structures such as the brainstem and the subcortical gray region due to the increased probability of including non-target structures within those Talairach-defined regions.

Pearson R correlations (between gold standard and Talairach volumes) ranged from 0.77 for the brainstem to 0.96 for the frontal lobe and 0.95 for the temporal lobe. As expected, intraclass correlations (ICC) were lower than Pearson R values overall. However, the discrepancies between ICC and R values were much greater for small brain regions, such as the brainstem, cerebellar and subcortical gray regions. Whereas ICCs reached 0.86 for the frontal lobe and 0.90 for the temporal lobe, they were very low for the brainstem and the subcortical gray regions (0.00), and moderately low for the cerebellum (0.50). The ICC takes absolute volume differences between paired variables into account as well as the correlation between these values, and therefore was affected by the consistent volume differences in small re-

Table 1
Sensitivity, specificity, positive predictive value (PPV), intraclass correlation (ICC) and Pearson R for revised Talairach-based measurements of regions of interest in normal sample (means ± S.D.)

	Normal children ($N = 10$)	Normal adults ($N = 5$)	Normal sample ($N = 15$)
Frontal lobe			
Sensitivity	0.91 ± 0.02	0.88 ± 0.03	0.90 ± 0.02
Specificity	0.97 ± 0.01	0.98 ± 0.01	0.98 ± 0.01
PPV	0.95 ± 0.02	0.96 ± 0.01	0.95 ± 0.02
ICC	0.91	0.77	0.86
R	0.98	0.95	0.96
Parietal lobe			
Sensitivity	0.87 ± 0.02	0.89 ± 0.01	0.88 ± 0.02
Specificity	0.96 ± 0.01	0.95 ± 0.01	0.95 ± 0.01
PPV	0.85 ± 0.03	0.82 ± 0.04	0.84 ± 0.04
ICC	0.91	0.70	0.84
R	0.91	0.89	0.88
Occipital lobe			
Sensitivity	0.86 ± 0.03	0.88 ± 0.03	0.86 ± 0.03
Specificity	0.98 ± 0.01	0.98 ± 0.00	0.98 ± 0.00
PPV	0.82 ± 0.04	0.83 ± 0.03	0.82 ± 0.04
ICC	0.74	0.76	0.73
R	0.80	0.93	0.81
Temporal lobe			
Sensitivity	0.86 ± 0.03	0.85 ± 0.02	0.86 ± 0.02
Specificity	0.98 ± 0.01	0.98 ± 0.01	0.98 ± 0.00
PPV	0.89 ± 0.02	0.91 ± 0.02	0.89 ± 0.02
ICC	0.93	0.88	0.90
R	0.96	0.96	0.95
Brainstem			
Sensitivity	0.95 ± ± 03	0.94 ± 0.02	0.95 ± 0.02
Specificity	0.99 ± 0.00	0.99 ± 0.00	0.99 ± 0.00
PPV	0.59 ± 0.06	0.63 ± 0.04	0.60 ± 0.05
ICC	0.00	0.00	0.00
R	0.73	0.90	0.77
Cerebellum			
Sensitivity	0.82 ± 0.03	0.85 ± 0.03	0.83 ± 0.03
Specificity	0.99 ± 0.00	0.99 ± 0.00	0.99 ± 0.00
PPV	0.94 ± 0.03	0.92 ± 0.02	0.93 ± 0.03
ICC	0.44	0.72	0.50
R	0.93	0.96	0.89
Subcortical gray			
Sensitivity	0.85 ± 0.03	0.83 ± 0.02	0.85 ± 0.03
Specificity	0.98 ± 0.00	0.98 ± 0.00	0.98 ± 0.00
PPV	0.65 ± 0.03	0.64 ± 0.06	0.65 ± 0.04
ICC	0.00	0.00	0.00
R	0.89	0.66	0.85

gions between manually and Talairach-defined measurements, as illustrated in Table 2. Accordingly, the largest volume differences between the Talairach and manual measurements were found for the brainstem (mean percent difference ± S.D.: 59.4 ± 17.9). In contrast, the mean percent differences between gold standard and Talairach measures for the lobar regions were generally small: frontal lobe, −5.5 ± 4.8; occipital lobe, 5.7 ± 7.6; parietal lobe, 4.5 ± 6.7; and temporal lobe, −4.1 ± 4.0.

3.3. Applicability of revised Talairach definitions to an independent pediatric sample

Tables 3 and 4 illustrate the applicability of the revised Talairach definitions to an independent sample of girls with Rett syndrome. Compared to measurements based on the originally defined sectors, sensitivity, specificity, and positive predictive values either remained unchanged or increased as a result of revising the sectors to fit the brains of children. Sensitivity values were high for all brain regions, ranging from 0.79 for the subcortical gray region to 0.90 for the frontal lobe and 0.96 for the brainstem. Significant increases in sensitivity based on Talairach sector revisions were found for the parietal, occipital, and temporal lobes and the brainstem. The most dramatic change was found for the occipital lobe, which increased in sensitivity from 0.57 when based on originally defined sectors to 0.89 when based on revised sectors. Specificity was very high for measurements based on both the original and the revised sectors, ranging from 0.96 to 0.99. Although PPV increased significantly for the occipital lobe, the cerebellum and the subcortical gray region on the basis of Talairach sector revisions, values were not uniformly high, varying from 0.57 for the brainstem to 0.94 for the frontal lobe.

Correlations between gold standard and revised Talairach measures increased overall when calculated with the Pearson R. However, when the intraclass correlation was calculated, correlations decreased slightly for the occipital lobe and somewhat dramatically for the cerebellum. As is indicated in Table 4, reduced intraclass correlations for these regions are most likely related to the

fact that the total volumetric difference between the gold standard and the revised Talairach measurements was greater than the difference between the gold standard and original Talairach measurements for both the occipital lobe and the cerebellum. For all other brain regions (with the exception of the brainstem), the percent difference between the gold standard and Talairach measurements either remained unchanged or decreased slightly when the revised Talairach sectors were applied.

3.4. Preliminary validation of Talairach-defined measures

The validity of the automated method was assessed by comparing the automated measurements of regional brain volumes to gold standard measurements of healthy girls vs. healthy boys (see Table 2) and healthy girls vs. girls with Rett syndrome (see Tables 2 and 4). Since correlation coefficients (described above) were relatively low

Table 2
Volume measurements (cubic centimeters) and percent differences between gold standard and revised Talairach-defined regions of interest for normal sample (means ± S.D.)

	Normal boys ($N = 5$)	Normal girls ($N = 5$)	Normal adults ($N = 5$)	Normal sample ($N = 15$)
Frontal lobe				
Gold	491.2 ± 45.1	404.1 ± 36.5	453.9 ± 59.7	449.7 ± 59.1
Talairach	465.6 ± 40.8	390.7 ± 42.9	416.7 ± 53.8	424.3 ± 52.1
% Diff	−5.2 ± 2.9	−3.1 ± 3.3	−8.1 ± 3.8	−5.5 ± 4.8
Parietal lobe				
Gold	319.1 ± 41.1	268.2 ± 14.7	273.5 ± 35.4	286.9 ± 38.2
Talairach	327.4 ± 35.0	272.0 ± 21.3	297.6 ± 33.8	299.0 ± 36.8
% Diff	3.0 ± 6.3	1.4 ± 5.7	9.1 ± 6.5	4.5 ± 6.7
Occipital lobe				
Gold	139.3 ± 12.1	113.2 ± 5.2	126.5 ± 12.4	126.3 ± 14.8
Talairach	144.2 ± 13.6	121.2 ± 19.1	134.6 ± 19.1	133.3 ± 16.1
% Diff	3.9 ± 9.9	7.3 ± 6.8	6.1 ± 7.0	5.7 ± 7.6
Temporal lobe				
Gold	237.6 ± 24.5	196.7 ± 10.6	228.4 ± 34.7	220.9 ± 29.6
Talairach	229.2 ± 27.7	191.0 ± 12.5	214.7 ± 30.3	211.6 ± 28.1
% Diff	−3.6 ± 3.9	−2.9 ± 4.4	−5.9 ± 3.8	−4.1 ± 4.0
Brainstem				
Gold	30.4 ± 3.6	26.7 ± 1.8	35.0 ± 3.5	30.7 ± 4.5
Talairach	53.3 ± 2.6	40.4 ± 5.0	52.5 ± 5.7	48.7 ± 7.5
% Diff	77.0 ± 20.0	51.1 ± 9.5	50.0 ± 6.8	59.4 ± 17.9
Cerebellum				
Gold	152.5 ± 15.8	132.6 ± 8.8	141.3 ± 18.4	142.1 ± 16.2
Talairach	134.9 ± 15.8	112.6 ± 3.9	130.8 ± 12.8	126.2 ± 14.8
% Diff	−11.6 ± 3.0	−14.6 ± 5.2	−7.1 ± 4.2	−11.1 ± 5.1
Subcortical gray				
Gold	38.3 ± 3.2	31.3 ± 3.5	31.9 ± 1.2	33.8 ± 4.2
Talairach	50.8 ± 6.2	41.0 ± 1.8	41.6 ± 4.8	44.4 ± 6.3
% Diff	32.3 ± 7.8	32.0 ± 12.8	30.4 ± 12.6	31.6 ± 10.5

Table 3
Comparison of sensitivity, specificity, positive predictive value (PPV), intraclass correlation (ICC), and Pearson R between manual measurements and measurements based on original and revised Talairach-defined regions of interest in sample of five girls with Rett syndrome (means ± S.D.)

	Original Talairach sectors	Revised Talairach sectors	Z-Value[a]
Frontal lobe			
Sensitivity	0.89 ± 0.04	0.90 ± 0.03	
Specificity	0.97 ± 0.01	0.98 ± 0.01	
PPV	0.93 ± 0.01	0.94 ± 0.02	
ICC	0.76	0.77	
R	0.97	0.97	
Parietal lobe			
Sensitivity	0.73 ± 0.06	0.87 ± 0.01	−2.02*
Specificity	0.96 ± 0.02	0.96 ± 0.01	
PPV	0.83 ± 0.09	0.84 ± 0.04	
ICC	0.01	0.88	
R	0.27	0.95	
Occipital lobe			
Sensitivity	0.57 ± 0.28	0.89 ± 0.04	−2.02*
Specificity	0.97 ± 0.01	0.98 ± 0.01	
PPV	0.68 ± 0.07	0.78 ± 0.07	−2.02*
ICC	0.24	0.17	
R	0.17	0.54	
Temporal lobe			
Sensitivity	0.83 ± 0.02	0.85 ± 0.02	−2.02*
Specificity	0.95 ± 0.00	0.97 ± 0.01	
PPV	0.78 ± 0.02	0.86 ± 0.05	
ICC	0.48	0.72	
R	0.91	0.92	
Brainstem			
Sensitivity	0.80 ± 0.06	0.96 ± 0.02	−2.02*
Specificity	0.98 ± 0.01	0.98 ± 0.00	
PPV	0.56 ± 0.09	0.57 ± 0.03	
ICC	0.00	0.00	
R	0.56	0.87	
Cerebellum			
Sensitivity	0.87 ± 0.07	0.83 ± 0.04	
Specificity	0.97 ± 0.01	0.99 ± 0.00	−2.02*
PPV	0.82 ± 0.04	0.94 ± 0.02	−2.02*
ICC	0.56	0.31	
R	0.73	0.77	
Subcortical gray			
Sensitivity	0.75 ± 0.02	0.79 ± 0.03	
Specificity	0.98 ± 0.00	0.99 ± 0.00	−2.02*
PPV	0.68 ± 0.07	0.74 ± 0.04	−2.02*
ICC	0.52	0.66	
R	0.74	0.77	

[a] Sensitivity, specificity and PPV are compared with the Wilcoxon Signed Rank Test. Only significant Z-values are reported.
* $P \leq .05$

for the brainstem, subcortical regions and the cerebellum, we limited our comparisons to lobar regions. For both the Rett vs. normal girl analyses and the normal boy vs. normal girl analyses, we found group differences in the same direction for all lobes using either the automated or the gold standard method of measurement (results not shown).

4. Discussion

This study demonstrates that an automated, Talairach atlas-based parcellation method can be used to produce sensitive and specific volumetric measures of lobar brain regions in both normal children and children with a known disorder affecting brain development and morphology. In doing so, we have extended the findings of our previous study (Kaplan et al., 1997) in which this method was applied to the measurement of major anatomical structures (including the cerebrum, cerebellum and lateral ventricles) in a pediatric sample. Taking both studies together, the results support the methodological approach advocated by Andreasen et al. (1996), who reliably and validly applied this atlas-based parcellation procedure to the adult human brain. Accordingly, the findings of the current study suggest that more rapid and efficient derivation of volumetric measures of the major lobar regions of the child's brain are possible, thus allowing for finer-grained analysis of brain-behavior relations. Although the eventual goal of atlas-based measurement is to parcellate neurofunctional subregions of lobes (for example, the prefrontal dorsolateral and orbital frontal regions), recent findings of manually measured lobar differences between children with developmental disorders and unaffected peers (Piven et al., 1996) emphasize the usefulness of the current application of this method. The results suggest that the parcellation method is particularly useful for the automated measurement of the frontal, parietal and temporal lobes.

When the revised Talairach definitions were applied to a sample of children with a disorder that is known to affect the morphology of the brain, high levels of volumetric agreement, sensitivity, specificity and positive predictive values were obtained for relatively large lobar regions such as the frontal and temporal lobes. Although sensitivity and specificity were also high for

Table 4
Comparison of volume measurements (cubic centimeters) and percent differences between gold standard and original and revised Talairach-defined regions of interest for the Rett sample ($n = 5$) (means $\pm$ S.D.)

	Gold standard	Original Talairach sectors (% difference)	Revised Talairach sectors (% difference)
Frontal lobe	330.0 ± 20.1	315.2 ± 33.3 (-4.7 ± 4.7)	316.1 ± 32.9 (-4.4 ± 4.6)
Parietal lobe	222.3 ± 25.9	196.6 ± 18.5 (-10.8 ± 12.0)	228.3 ± 18.0 (3.1 ± 5.0)
Occipital lobe	93.4 ± 14.8	97.6 ± 11.2 (6.4 ± 20.0)	106.0 ± 7.7 (15.3 ± 16.1)
Temporal lobe	175.1 ± 9.8	186.7 ± 11.9 (6.7 ± 2.8)	170.7 ± 12.3 (-2.5 ± 3.1)
Brainstem	23.0 ± 2.8	33.5 ± 2.8 (46.2 ± 15.3)	38.4 ± 2.8 (67.7 ± 10.8)
Cerebellum	120.7 ± 10.6	129.0 ± 19.5 (6.6 ± 11.9)	107.5 ± 11.3 (-11.0 ± 6.0)
Subcortical gray	32.1 ± 4.5	35.5 ± 3.9 (11.3 ± 11.1)	34.5 ± 3.8 (8.1 ± 9.3)

smaller regions such as the brainstem and the subcortical region, positive predictive values and intraclass correlations were lower due to the discrepancy in absolute values between the Talairach-defined and gold standard ROIs, and the difficulty excluding non-target tissue from the Talairach-defined measures of those relatively small regions. This was particularly the case for the brainstem. (The relation between size of the target structure and positive predictive value corresponds to findings in the epidemiology literature, from which the concept is derived: as Gordis (1996), points out, the lower the prevalence of a disease, the lower the predictive value.)

These findings demonstrate the usefulness of including positive predictive values in an evaluation of the Talairach method. Positive predictive value is an index of spatial accuracy based on a ratio of the volume of the 'target' voxels to the volumes of all voxels included within the Talairach ROI. For spatial data, it is more meaningful than specificity as an indicator of how well the Talairach ROIs exclude non-target structures. Whereas specificity estimates the ratio of correctly excluded voxels to all non-target structures in the brain, positive predictive value estimates the ratio of correctly included voxels to all structures within the Talairach ROI itself. As the data demonstrate, specificity can be very high even if the Talairach ROI is not excluding a large percentage of non-target structures. We were able to achieve high levels of specificity, sensitivity and positive predictive value in part through our reassignment of approximately 10% of the sectors from the atlas defined by Andreasen and colleagues. Although reassignment of sectors did not significantly affect absolute differences in volumes, it did positively affect the configuration of sectors which led to higher values in sensitivity, specificity and PPV, which reflect not only volumetric differences but also spatial overlap. In the case of the occipital and frontal lobes, sector reassignment was based on what appeared to be differences in rules for manual measurement of the lobar regions. For example, 100% of the 18 sectors that were reassigned from the parietal lobe were assigned to the frontal lobe. This appeared to be due to differences in operational definitions for this region, in particular relating to delineation of the superior aspect of the posterior frontal lobe. The positive effect of reassignment of sectors was most evident in the occipital region. Thirty-six percent of the original occipital region was reassigned to other regions, thereby reducing the likelihood of including non-target structures within the Talairach-defined occipital lobe and resulting in a significant increase in PPV for the sample of children with Rett syndrome.

Exploratory analyses comparing girls with Rett syndrome to age-matched normal girls, and normal girls to normal boys, indicated that differences shown by revised Talairach-defined regions were comparable to differences revealed by analysis of gold standard regions. This preliminary evidence of convergent validity suggests that the Talairach-based parcellation method can be applied both to normal pediatric study groups and children with a brain disorder that severely affects brain morphology.

Generalizability of the results is limited to some extent by the fact that the revision of Talairach sectors was based on our revisions of Andreasen's manual tracings of lobar regions. As such, it is not surprising that we achieved higher sensitivity and specificity between our manual tracings and our revised Talairach sectors than between our manual tracings and the sectors proposed by Andreasen and colleagues. Although the application of our revised method to a sample of girls with Rett syndrome allowed us to test the method on brains with significantly altered brain morphology, the small size of the sample is a further limitation. Accordingly, future studies, currently in progress, will test the applicability of this method on a broader range of pediatric disease groups, using larger samples across a wider age span and IQ range. The present findings, however, emphasize the important potential that this method holds for developing an automated, quantitative atlas of brain development for both normal children and children with brain disorders.

The results described here suggest that the use of an atlas-based parcellation method has several advantages over a method of parcellation based

on the manual identification and delineation of sulcal and gyral (Rademacher et al., 1992) boundaries. The use of a stereotactic atlas standardizes both the position of the brain and the neuroanatomic location of large brain regions. By standardizing the Talairach-specific sectors that fall into each lobe, the atlas can be applied not only to structural imaging studies but to pediatric functional imaging modalities as well. Moreover, although the initial task of sector assignment relies on a great deal of neuroanatomic expertise (Andreasen et al., 1996), semi-automated atlas-based measurements can be completed by personnel without the high level of training required by manual measurement protocols. Manual boundary tracing protocols require labor-intensive, time-consuming efforts, in contrast to the stereotactic method which allows for the rapid and reliable measurement of brain regions in relatively large numbers of research participants. This can contribute more rapidly to the accumulation of much needed research knowledge of quantitative neurodevelopment in both normal and diseased pediatric populations.

The automated atlas-based parcellation method has limitations, however, which make the manual parcellation of brain regions using gyral and sulcal patterns more appropriate for answering a particular subset of research questions (Aylward et al., 1997). The manual method allows the investigator to identify inter- and intra-individual anatomic variability, including lateral asymmetry and anomalies of the cortical surface, both of which have been found in specific pediatric disease/disorder groups (Piven et al., 1990; Castellanos et al., 1996). Moreover, variation in brain shape, location of major sulci (Ono et al., 1990), and lack of proportionality between brain regions can be identified more readily through manual tracing methods. In addition, manual measurement appears to be more accurate for small neuroanatomic structures (Andreasen et al., 1996; Kaplan et al., 1997) and structures that border several neuroanatomic regions. Although the application of the method appears useful for relatively large lobar brain regions (particularly frontal, parietal and temporal regions), the large volumetric differences between the manual and Talairach measures found for the brainstem, the cerebellum and the subcortical region, for example, greatly diminish the utility of the current Talairach grid for the measurement of relatively small structures.

One approach to measuring small structures with the automated method is to revise the Talairach atlas further by subdividing sectors so that a higher level of spatial accuracy could be achieved for relatively small structures. Smaller Talairach sectors would improve spatial accuracy by minimizing the inclusion of non-target areas within the Talairach-defined region. Presumably, this would improve positive predictive values, and ICCs between manual and Talairach-defined measurements. Accordingly, the initial investment of the high level of neuroanatomic expertise that would be required to do this would 'pay off' in the increased speed and efficiency with which these structures could be measured. Subdivision of sectors would also facilitate the subparcellation and measurement of regions of interest within cerebral lobes, another current limitation of the automated method. Automated subparcellation of neurofunctional ROIs within lobes (such as the dorsolateral prefrontal cortex and the inferior parietal lobe) would permit specific analysis of brain and behavior relations not currently feasible with the automated procedure.

In contrast to automated non-linear approaches to spatial measurement (Christensen et al., 1994; Collins et al., 1994), the linear parcellation method described here is also limited in its capacity to incorporate normal variation in the convexity of the cortical surface into its measurements. However, at this time, non-linear methods require massive computation time and cannot be implemented on desktop computers. For current clinical studies, therefore, the linear-based approach is more efficient.

Even with its current limitations, the automated parcellation method described here is a powerful tool for measuring lobar regions of the brain in a rapid and reliable manner. It is an effective tool for identifying structures that may be promising targets for further subparcellation

and measurement. We have demonstrated that this tool can be applied as effectively to children as to adults, suggesting that the atlas-based automated method of measurement holds much promise for facilitating pediatric neuroimaging research.

Acknowledgements

This research was supported in part by NIH Grants MH01142, MH50047, HD24448, and HD31715 (RO1 and supplement to Dr Kates).

Appendix A. Protocol for the manual measurement of cerebral lobes, brainstem, cerebellum, and subcortical region

The following manual measurement rules were used to delineate each structure.

Frontal lobe: Initially, the central sulcus is identified in relation to several morphological landmarks on a three-dimensional rendered image of the cortical surface of the brain. For example, the superior temporal gyrus is followed to the supramarginal gyrus, which terminates at the postcentral sulcus. The superior and medial frontal gyri are followed to their termination at the precentral gyrus. The operculum, which corresponds to the inferior frontal gyrus and is immediately anterior to the precentral gyrus, is also identified (Fig. 2). Once the central sulcus is identified on the rendered surface of the brain, the rater attempts to identify the central sulcus on the coronal stack. The sulcus usually becomes visible posterior to the appearance of the anterior commissure. The rater draws small seeds on the points where the central sulcus intersects the lateral edge of each coronal slice. If the central sulcus intersects the coronal slice twice, then the inferior point of intersection is chosen as the lower boundary of the frontal lobe, and a seed is placed at that point. The rater fills all seeds with white, and renders the image to reveal the surface of the brain. If the seeds are placed correctly on the coronal slices, they will delineate the location of the central sulcus when the surface of the brain is rendered.

Once the central sulcus is confirmed on coronal slices, the entire frontal lobe can be traced. In the anterior region of the brain, the boundaries of the frontal lobe are defined by the cortical surface, which can be demarcated from surrounding

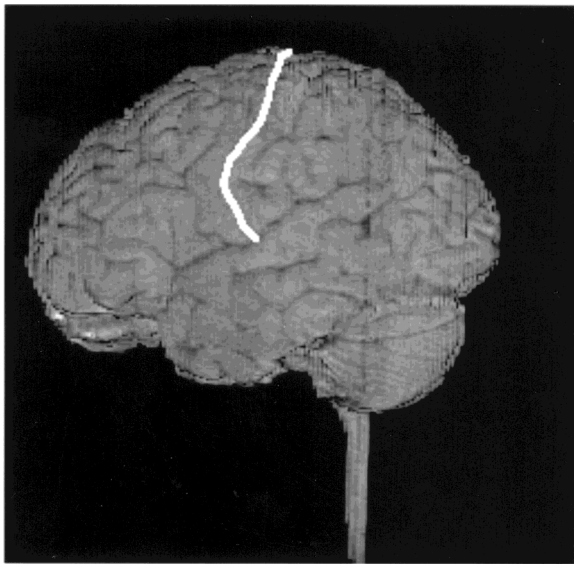

Fig. 2. A three-dimensional rendered image of the cortical surface of the brain, with the central sulcus delineated in white.

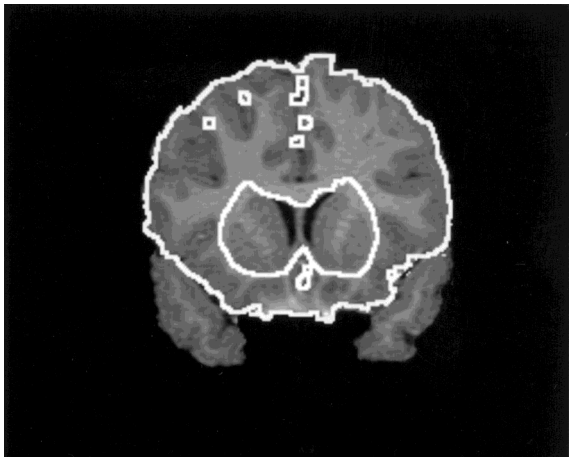

Fig. 3. The manual tracing of the frontal lobe at the level of the basal ganglia.

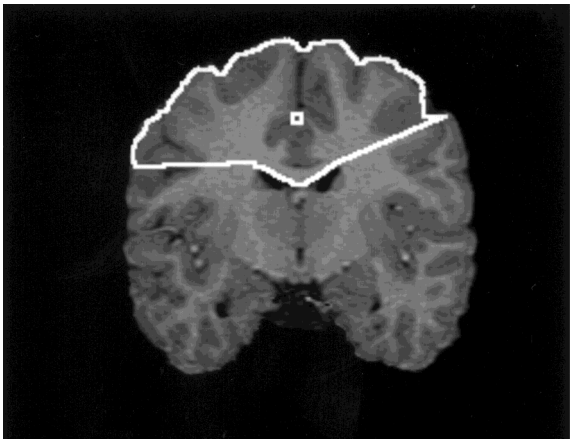

Fig. 4. The manual tracings of the frontal lobe based on the intersection of the central sulcus with the lateral aspect of the brain, moving posteriorly through the coronal plane.

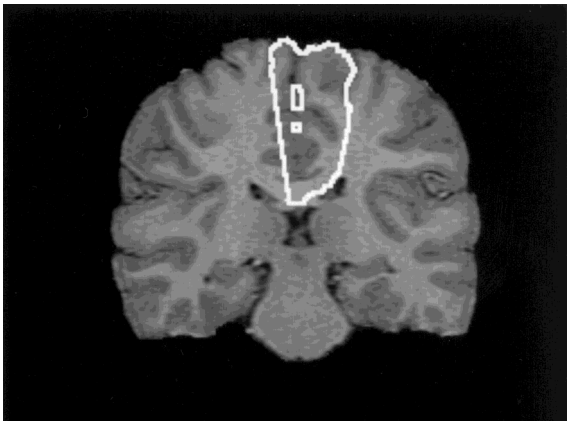

Fig. 6. The manual tracings of the frontal lobe based on the intersection of the central sulcus with the lateral aspect of the brain, moving posteriorly through the coronal plane.

CSF by automated edge detection tools. As the coronal view progresses posteriorly, and the temporal lobe appears, the inferior boundary for the frontal lobe is the sylvian fissure (Fig. 3). At the level of the basal ganglia, lateral ventricles and subcortical tissue (containing the caudate nucleus, putamen and claustrum) are excluded from the frontal lobe. At the level at which the seeds marking the central sulcus appear, the inferior border of the frontal lobe is formed by a line that is drawn from the depth of the central sulcus to the inferior aspect of the corpus callosum, across the interhemispheric fissure, to the lateral edge of the central sulcus on the contralateral side. All tissue superior to that line is included in the measurement of the frontal lobe. The frontal lobe continues to be traced until the central sulcus is no longer discernible in the coronal view (Figs. 4–6).

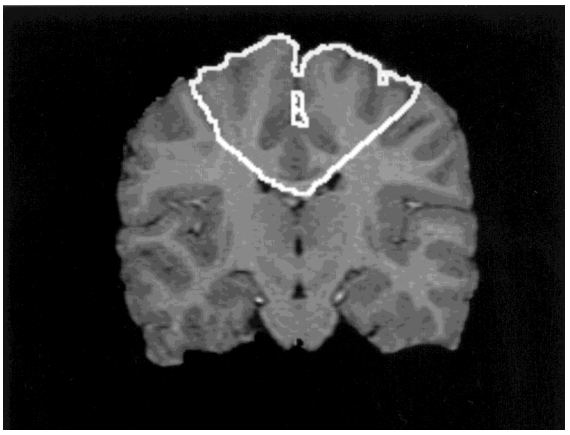

Fig. 5. The manual tracings of the frontal lobe based on the intersection of the central sulcus with the lateral aspect of the brain, moving posteriorly through the coronal plane.

Temporal lobe: In the anterior region of the temporal lobe, the lateral, medial and inferior borders of the temporal lobe are the cortical surface of the brain. In the mesial region of the temporal lobe, the medial and inferio-medial borders of the temporal lobe consist of the brainstem and the cerebellum. The superior border of the temporal lobe consists of the sylvian fissure, and a line connecting the furthest extent of the inferior ramus of the sylvian fissure to the choroidal fissure (Figs. 7–9). The sylvian fissure marks the superior border of the temporal lobe until the slice just prior to the distinct appearance of the ascending fornix in the collateral trigone. Posterior to this level, the sylvian fissure is no longer distinct. Subsequently, the lateral superior border continues to be drawn at the same level as the last slice containing the sylvian fissure (i.e. the same x coordinate), but as a straight line extending to the superior border of the parahippocam-

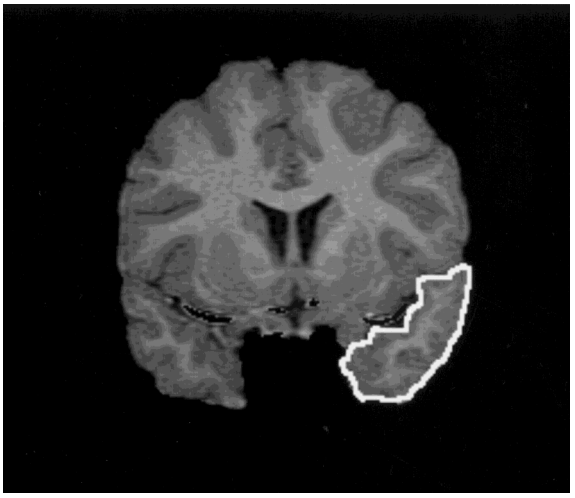

Fig. 7. The manual tracings of the temporal lobe, moving posteriorly through the coronal plane.

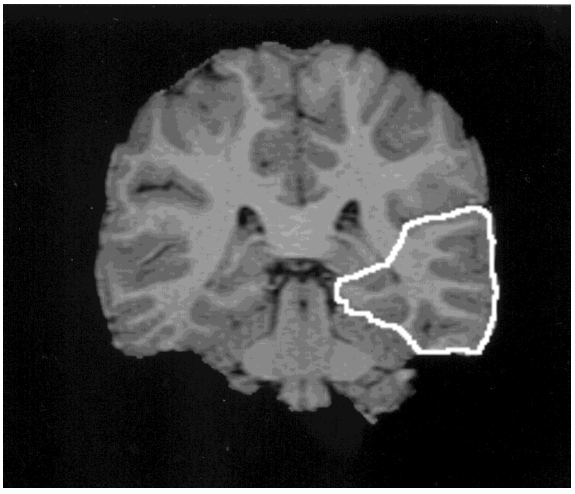

Fig. 9. The manual tracings of the temporal lobe, moving posteriorly through the coronal plane.

pal gyrus. (The isthmus, which is the structure located beneath the corpus callosum and above the parahippocampal gyrus, is excluded. When the corpus callosum is visible and the isthmus is adjacent to the hippocampus, the isthmus is the gyrus-like protruding gray matter. The ROI excludes this protrusion, continues to the top of the hippocampus, and then extends a straight line to the superior lateral border.) The posterior boundary of the temporal lobe is contiguous with and defined by the anterior boundary of the occipital lobe.

Occipital lobe: The lateral and caudal borders of the occipital lobe are all defined by the cortical

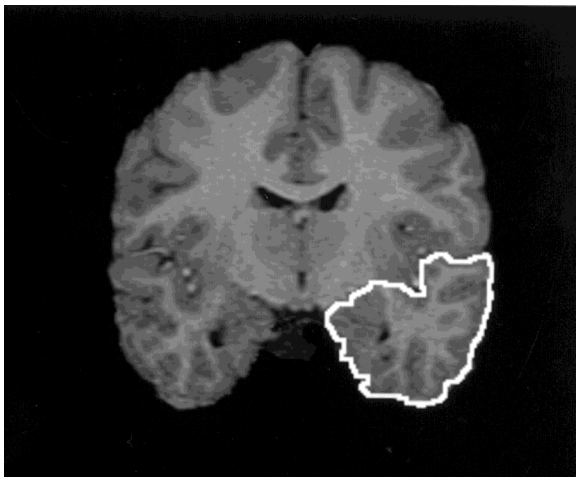

Fig. 8. The manual tracings of the temporal lobe, moving posteriorly through the coronal plane.

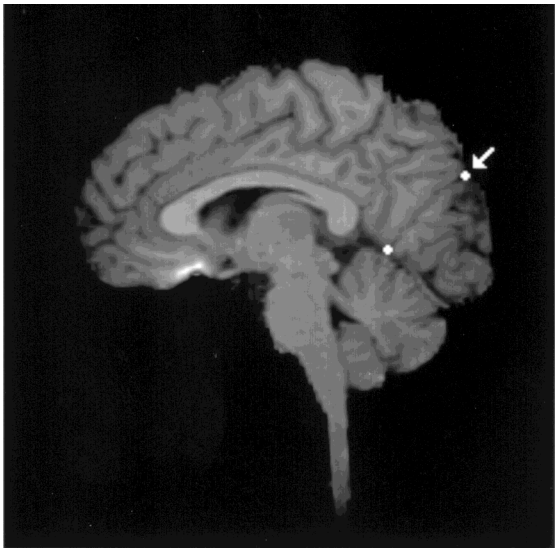

Fig. 10. The inferior and superior points of the medial parietal–occipital sulcus.

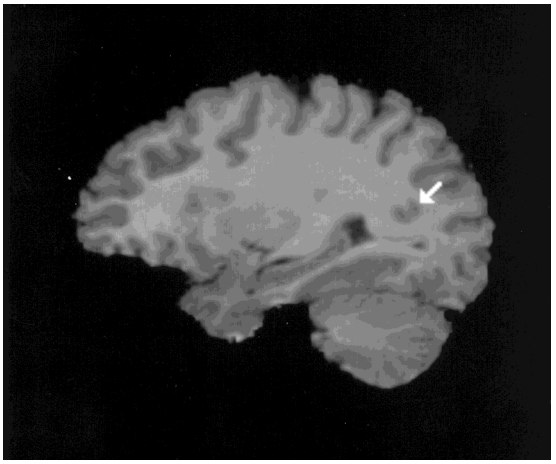

Fig. 11. The lateral parietal–occipital sulcus.

surfaces of the brain. Medially each hemisphere of the lobe extends to the interhemispheric fissure. Inferiorly the occipital lobe is separated from the cerebellum via the tentorium. We used four landmarks to set up two flat cutting planes defining the rostral border of the occipital lobe. The first and second landmarks are the inferior and superior points (respectively) of the most medial and well-defined parietal–occipital sulcus (Fig. 10). The third point is the furthest lateral extent of the parieto–occipital sulcus as we progress from a midsagittal position toward the

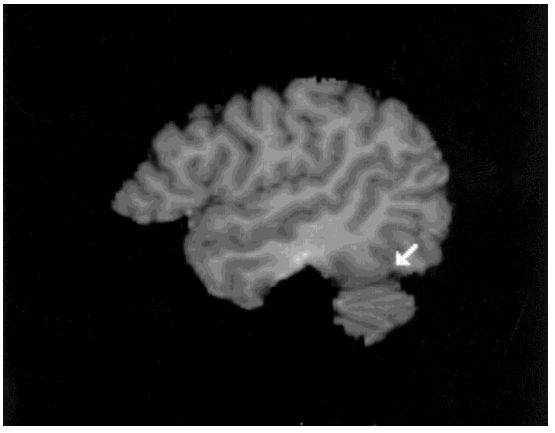

Fig. 12. The pre-occipital notch.

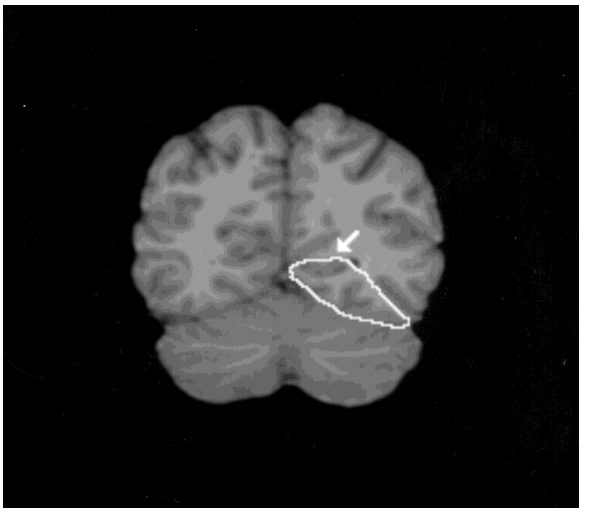

Fig. 13. The calcarine region of the occipital lobe (Brodmann Area 17).

cortical surface (Fig. 11). These first three points define a plane demarcating the rostral border of the occipital lobe on the medial half of the brain. The more lateral half of the occipital lobe is defined rostrally by the lateral edge of this two-di-

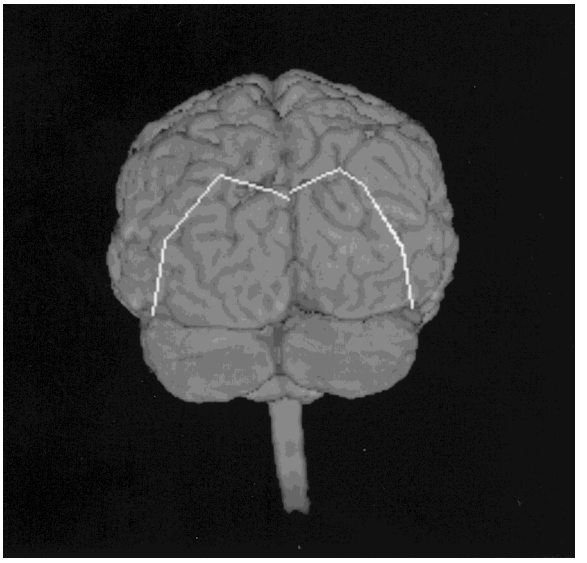

Fig. 14. The rendered surface of the posterior aspect of the brain, highlighting the occipital lobe.

mensional plane and a fourth landmark, the (pre)occipital notch just medial to the lateral surface of the cerebellum (Fig. 12).

After the rostral borders of the occipital lobe have been created, the brain is reoriented back into standard AC-PC space and any newly defined tissue occurring anterior to the splenium of the corpus collosum is omitted. Additionally the occipital lobe is edited manually to include surrounding Area 17 (Brodmann). After finding the most anterior point of the calcarine sulcus which is posterior to the splenium, tissue is added superiorly by following the contour of the superior gray matter surrounding the calcarine sulcus (Fig. 13). All gray matter exclusively associated with the calcarine cortex should be incorporated within the edited tissue. This also means that white matter located inferior to the calcarine sulcus will also be included. When the calcarine gray matter is indistinguishable from other more superior gray matter, it should be excluded from occipital tissue. In the coronal view the edited occipital tissue progresses laterally to the end of this calcarine gray matter or to the originally defined borders, whichever is most lateral (Fig. 14).

Parietal lobe: This region included all remaining cortical sectors not assigned to the frontal, occipital or temporal lobes.

Subcortical region: This region was delineated by initially filling in the frontal, temporal, and occipital lobes, and the brainstem and cerebellum. The demarcation of the subcortical region was marked by drawing an ROI tangent to the edge of each of the structures listed above. Subsequently, the subcortical region was carved out by including the lateral ventricles, the caudate, the internal capsule, the putamen, the external capsule and the claustrum.

Brainstem and cerebellum: These regions were delineated on axial slices, using previously established rules (Aylward and Reiss, 1991; Reiss et al., 1995).

Appendix B. Complete list of Talairach sectors by brain region

Brainstem

E2aL10, E2aL11, E2aL12, E2aL13, E2aL9, E2aR10, E2aR11, E2aR12, E2aR13, E2aR9, E3aL10, E3aL11, E3aL12, E3aL13, E3aL14, E3aL9, E3aR10, E3aR11, E3aR12, E3aR13, E3aR14, E3aR9, FaL10, FaL11, FaL12, FaL13, FaL14, FaL9, FaR10, FaR11, FaR12, FaR13, FaR14, FaR9

Cerebellum

E3bL13, E3bR13, FbL11, FbL12, FbL13, FbL14, FbR11, FbR12, FbR13, FbR14, FcL11, FcL12, FcL13, FcL14, FcR11, FcR12, FcR13, FcR14, FdL12, FdL13, FdR12, FdR13, GaL10, GaL11, GaL12, GaL13, GaL14, GaR10, GaR11, GaR12, GaR13, GaR14, GbL10, GbL11, GbL12, GbL13, GbL14, GbR10, GbR11, GbR12, GbR13, GbR14, GcL11, GcL12, GcL13, GcL14, GcR11, GcR12, GcR13, GcR14, GdL11, GdL12, GdL13, GdL14, GdR11, GdR12, GdR13, GdR14, HaL10, HaL11, HaL12, HaL13, HaL14, HaR10, HaR11, HaR12, HaR13, HaR14, HbL11, HbL12, HbL13, HbL14, HbR11, HbR12, HbR13, HbR14, HcL11, HcL12, HcL13, HcL14, HcR11, HcR12, HcR13, HcR14, IaL11, IaL12, IaL13, IaR11, IaR12, IaR13, IbL11, IbL12, IbL13, IbR11, IbR12, IbR13, IcL11, IcL12, IcL13, IcR11, IcR12, IcR13

Frontal lobe

AaL10, AaL11, AaL2, AaL3, AaL4, AaL5, AaL6, AaL7, AaL8, AaL9, AaR10, AaR11, AaR2, AaR3, AaR4, AaR5, AaR6, AaR7, AaR8, AaR9, AbL10, AbL11, AbL2, AbL3, AbL4, AbL5, AbL6, AbL7, AbL8, AbL9, AbR10, AbR11, AbR2, AbR3, AbR4, AbR5, AbR6, AbR7, AbR8, AbR9, AcL10, AcL11, AcL2, AcL3, AcL4, AcL5, AcL6, AcL7, AcL8, AcL9, AcR10, AcR11, AcR2, AcR3, AcR4, AcR5, AcR6, AcR7, AcR8, AcR9, AdL10, AdL11, AdL2, AdL3, AdL4, AdL5, AdL6, AdL7, AdL8, AdL9, AdR10, AdR11, AdR2, AdR3, AdR4, AdR5, AdR6, AdR7, AdR8, AdR9, BaL10, BaL11, BaL2, BaL3, BaL4, BaL5, BaL6, BaL7, BaL8, BaL9, BaR10, BaR11, BaR2, BaR3, BaR4, BaR5, BaR6, BaR7, BaR8,

BaR9, BbL10, BbL11, BbL2, BbL3, BbL4, BbL5, BbL6, BbL7, BbL8, BbL9, BbR10, BbR11, BbR2, BbR3, BbR4, BbR5, BbR6, BbR7, BbR8, BbR9, BcL10, BcL11, BcL2, BcL3, BcL4, BcL5, BcL6, BcL7, BcL8, BcL9, BcR10, BcR11, BcR2, BcR3, BcR4, BcR5, BcR6, BcR7, BcR8, BcR9, BdL10, BdL11, BdL2, BdL3, BdL4, BdL5, BdL6, BdL7, BdL8, BdL9, BdR10, BdR11, BdR2, BdR3, BdR4, BdR5, BdR6, BdR7, BdR8, BdR9, CaL1, CaL10, CaL11, CaL2, CaL3, CaL4, CaL5, CaL6, CaL7, CaL8, CaL9, CaR1, CaR10, CaR11, CaR2, CaR3, CaR4, CaR5, CaR6, CaR7, CaR8, CaR9, CbL1, CbL10, CbL2, CbL3, CbL4, CbL5, CbL6, CbL7, CbL8, CbL9, CbR1, CbR10, CbR2, CbR3, CbR4, CbR5, CbR6, CbR7, CbR8, CbR9, CcL1, CcL2, CcL3, CcL4, CcL5, CcL6, CcL7, CcL8, CcL9, CcR1, CcR2, CcR3, CcR4, CcR5, CcR6, CcR7, CcR8, CcR9, CdL1, CdL2, CdL3, CdL4, CdL5, CdL6, CdL7, CdL8, CdL9, CdR1, CdR2, CdR3, CdR4, CdR5, CdR6, CdR7, CdR8, CdR9, DaL1, DaL10, DaL2, DaL3, DaL4, DaL5, DaL6, DaR1, DaR10, DaR2, DaR3, DaR4, DaR5, DaR6, DbL1, DbL2, DbL3, DbL4, DbL5, DbL6, DbR1, DbR2, DbR3, DbR4, DbR5, DbR6, DcL1, DcL2, DcL3, DcL4, DcL5, DcL6, DcL7, DcL8, DcR1, DcR2, DcR3, DcR4, DcR5, DcR6, DcR7, DcR8, DdL1, DdL2, DdL3, DdL4, DdL5, DdL6, DdL7, DdL8, DdR1, DdR2, DdR3, DdR4, DdR5, DdR6, DdR7, DdR8, E1aL1, E1aL2, E1aL3, E1aL4, E1aL5, E1aR1, E1aR2, E1aR3, E1aR4, E1aR5, E1bL1, E1bL2, E1bL3, E1bL4, E1bL5, E1bL6, E1bR1, E1bR2, E1bR3, E1bR4, E1bR5, E1bR6, E1cL1, E1cL2, E1cL3, E1cL4, E1cL5, E1cL6, E1cR1, E1cR2, E1cR3, E1cR4, E1cR5, E1cR6, E1dL1, E1dL2, E1dL3, E1dL4, E1dL5, E1dL6, E1dL7, E1dR1, E1dR2, E1dR3, E1dR4, E1dR5, E1dR6, E1dR7, E2aL1, E2aL2, E2aL3, E2aL4, E2aL5, E2aR1, E2aR2, E2aR3, E2aR4, E2aR5, E2bL1, E2bL2, E2bL3, E2bL4, E2bL5, E2bR1, E2bR2, E2bR3, E2bR4, E2bR5, E2cL1, E2cL2, E2cL3, E2cL4, E2cR1, E2cR2, E2cR3, E2cR4, E2dL1, E2dL2, E2dL3, E2dR1, E2dR2, E2dR3, E3aL1, E3aL2, E3aL3, E3aL4, E3aL5, E3aL6, E3aR1, E3aR2, E3aR3, E3aR4, E3aR5, E3aR6, E3bL1, E3bL2, E3bL3, E3bL4, E3bR1, E3bR2, E3bR3, E3bR4, E3cL1, E3cL2, E3cR1, E3cR2, FaL1, FaL2, FaL3, FaR1, FaR2, FaR3

Null

AaL1, AaL12, AaL13, AaL14, AaR1, AaR12, AaR13, AaR14, AbL1, AbL12, AbL13, AbL14, AbR1, AbR12, AbR13, AbR14, AcL1, AcL12, AcL13, AcL14, AcR1, AcR12, AcR13, AcR14, AdL1, AdL12, AdL13, AdL14, AdR1, AdR12, AdR13, AdR14, BaL1, BaL12, BaL13, BaL14, BaR1, BaR12, BaR13, BaR14, BbL1, BbL12, BbL13, BbL14, BbR1, BbR12, BbR13, BbR14, BcL1, BcL12, BcL13, BcL14, BcR1, BcR12, BcR13, BcR14, BdL1, BdL12, BdL13, BdL14, BdR1, BdR12, BdR13, BdR14, CaL12, CaL13, CaL14, CaR12, CaR13, CaR14, CbL13, CbL14, CbR13, CbR14, CcL13, CcL14, CcR13, CcR14, CdL13, CdL14, CdR13, CdR14, DaL13, DaL14, DaR13, DaR14, DbL13, DbL14, DbR13, DbR14, DcL13, DcL14, DcR13, DcR14, DdL13, DdL14, DdR13, DdR14, E1aL13, E1aL14, E1aR13, E1aR14, E1bL13, E1bL14, E1bR13, E1bR14, E1cL13, E1cL14, E1cR13, E1cR14, E1dL13, E1dL14, E1dR13, E1dR14, E2aL14,E2aR14, E2bL13, E2bL14, E2bR13, E2bR14, E2cL13, E2cL14, E2cR13, E2cR14, E2dL13, E2dL14, E2dR13, E2dR14, E3bL14, E3bR14, E3cL13, E3cL14, E3cR13, E3cR14, E3dL13, E3dL14, E3dR13, E3dR14, FdL14, FdR14, HaL1, HaR1, HbL1, HbR1, HcL1, HcR1, HdL1, HdL11, HdL12, HdL13, HdL14, HdL2, HdL3, HdR1, HdR11, HdR12, HdR13, HdR14, HdR2, HdR3, IaL1, IaL14, IaL2, IaL3, IaR1, IaR14, IaR2, IaR3, IbL1, IbL14, IbL2, IbL3, IbR1, IbR14, IbR2, IbR3, IcL1, IcL14, IcL2, IcL3, IcR1, IcR14, IcR2, IcR3, IdL1, IdL10, IdL11, IdL12, IdL13, IdL14, IdL2, IdL3, IdL4, IdL5, IdL6, IdL7, IdL8, IdL9, IdR1, IdR10, IdR11, IdR12, IdR13, IdR14, IdR2, IdR3, IdR4, IdR5, IdR6, IdR7, IdR8, IdR9

Occipital lobe

IcL5, IcR4, GaL8, GaR8, GbL9, GbR9, HaL6, HaL7, HaL8, HaL9, HaR6, HaR7, HaR8, HaR9, HbL10, HbL6, HbL7, HbL8, HbL9, HbR10, HbR6, HbR7, HbR8, HbR9, HcL10, HcL9, HcR10, HcR9, IaL10, IaL4, IaL5, IaL6, IaL7, IaL8, IaL9, IaR0, IaR4, IaR5, IaR6, IaR7, IaR8, IaR9, IbL10, IbL4, IbL5, IbL6, IbL7, IbL8, IbL9, IbR10, IbR5, IbR6, IbR7, IbR8, IbR9, IcL10, IcL4, IcL6, IcL7, IcL8, IcL9, IcR10, IcR5, IcR6, IcR7, IcR8, IcR9, GaL9, GaR9, GbL8, GbR8, IbR4

Parietal lobe

E1cL7, E1cL8, E1cR7, E1cR8, E2bL6, E2bR6, E2cL5, E2cL6, E2cL7, E2cR5, E2cR6, E2cR7, E2dL4, E2dL5, E2dL6, E2dL7, E2dR4, E2dR5, E2dR6, E2dR7, E3bL5, E3bL6, E3bR5, E3bR6, E3cL3, E3cL4, E3cL5, E3cL6, E3cL7, E3cR3, E3cR4, E3cR5, E3cR6, E3cR7, E3dL1, E3dL2, E3dL3, E3dL4, E3dL5, E3dL6, E3dR1, E3dR2, E3dR3, E3dR4, E3dR5, E3dR6, FaL4, FaL5, FaL6, FaL7, FaR4, FaR5, FaR6, FaR7, FbL1, FbL2, FbL3, FbL4, FbL5, FbL6, FbL7, FbR1, FbR2, FbR3, FbR4, FbR5, FbR6, FbR7, FcL1, FcL2, FcL3, FcL4, FcL5, FcL6, FcL7, FcR1, FcR2, FcR3, FcR4, FcR5, FcR6, FcR7, FdL1, FdL2, FdL3, FdL4, FdL5, FdL6, FdR1, FdR2, FdR3, FdR4, FdR5, FdR6, GaL1, GaL2, GaL3, GaL4, GaL5, GaL6, GaL7, GaR1, GaR2, GaR3, GaR4, GaR5, GaR6, GaR7, GbL1, GbL2, GbL3, GbL4, GbL5, GbL6, GbL7, GbR1, GbR2, GbR3, GbR4, GbR5, GbR6, GbR7, GcL1, GcL2, GcL3, GcL4, GcL5, GcL6, GcL7, GcR1, GcR2, GcR3, GcR4, GcR5, GcR6, GcR7, GdL1, GdL2, GdL3, GdL4, GdL5, GdL6, GdR1, GdR2, GdR3, GdR4, GdR5, GdR6, HaL2, HaL3, HaL4, HaL5, HaR2, HaR3, HaR4, HaR5, HbL2, HbL3, HbL4, HbL5, HbR2, HbR3, HbR4, HbR5, HcL2, HcL3, HcL4, HcL5, HcL6, HcL7, HcR2, HcR3, HcR4, HcR5, HcR6, HcR7, HdL4, HdL5, HdL6, HdR4, HdR5, HdR6

Subcortical region

DbL7, DbR7, E3bR7, DaL7, DaL8, DaL9, DaR7, DaR8, DaR9, DbL8, DbL9, DbR8, DbR9, E1aL6, E1aL7, E1aL8, E1aL9, E1aR6, E1aR7, E1aR8, E1aR9, E1bL7, E1bL8, E1bL9, E1bR7, E1bR8, E1bR9, E2aL6, E2aL7, E2aL8, E2aR6, E2aR7, E2aR8, E2bL7, E2bL8, E2bL9, E2bR7, E2bR8, E2bR9, E3aL7, E3aL8, E3aR7, E3aR8, E3bL7, E3bL8, E3bR8, FaL8, FaR8, FbL8, FbR8

Temporal lobe

CbL11, CbL12, CbR11, CbR12, CcL10, CcL11, CcL12, CcR10, CcR11, CcR12, CdL10, CdL11, CdL12, CdR10, CdR11, CdR12, DaL11, DaL12, DaR11, DaR12, DbL10, DbL11, DbL12, DbR10, DbR11, DbR12, DcL10, DcL11, DcL12, DcL9, DcR10, DcR11, DcR12, DcR9, DdL10, DdL11, DdL12, DdL9, DdR10, DdR11, DdR12, DdR9, E1aL10, E1aL11, E1aL12, E1aR10, E1aR11, E1aR12, E1bL10, E1bL11, E1bL12, E1bR10, E1bR11, E1bR12, E1cL10, E1cL11, E1cL12, E1cL9, E1cR10, E1cR11, E1cR12, E1cR9, E1dL10, E1dL11, E1dL12, E1dL8, E1dL9, E1dR10, E1dR11, E1dR12, E1dR8, E1dR9, E2bL10, E2bL11, E2bL12, E2bR10, E2bR11, E2bR12, E2cL10, E2cL11, E2cL12, E2cL8, E2cL9, E2cR10, E2cR11, E2cR12, E2cR8, E2cR9, E2dL10, E2dL11, E2dL12, E2dL8, E2dL9, E2dR10, E2dR11, E2dR12, E2dR8, E2dR9, E3bL10, E3bL11, E3bL12, E3bL9, E3bR10, E3bR11, E3bR12, E3bR9, E3cL10, E3cL11, E3cL12, E3cL8, E3cL9, E3cR10, E3cR11, E3cR12, E3cR8, E3cR9, E3dL10, E3dL11, E3dL12, E3dL7, E3dL8, E3dL9, E3dR10, E3dR11, E3dR12, E3dR7, E3dR8, E3dR9, FbL10, FbL9, FbR10, FbR9, FcL10, FcL8, FcL9, FcR10, FcR8, FcR9, FdL10, FdL11, FdL7, FdL8, FdL9, FdR10, FdR11, FdR7, FdR8, FdR9, GcL10, GcL8, GcL9, GcR10, GcR8, GcR9, GdL10, GdL7, GdL8, GdL9, GdR10, GdR7, GdR8, GdR9, HcL8, HcR8, HdL10, HdL7, HdL8, HdL9, HdR10, HdR7, HdR8, HdR9

References

Andreasen, N.C., Flashman, L., Flaum, M., Arndt, S., Swayze, V., O'Leary, D.S., Ehrhardt, J.C., Yuh, W.T.C., 1994. Regional brain abnormalities in schizophrenia measured with magnetic resonance imaging. Journal of the American Medical Association 272, 1763–1769.

Andreasen, N.C., Rajarethinam, R., Cizadlo, T., Arndt, S., Swayze, V.W., Flashman, L.A. II, O'Leary, D.S., Ehrhardt, J.C., Yuh, W.T.C., 1996. Automatic atlas-based volume estimation of human brain regions from MR images. Journal of Computer Assisted Tomography 20, 98–106.

Aylward, E.H., Reiss, A.L., 1991. Area and volume measurement of posterior fossa structures in MRI. Journal of Psychiatric Research 25, 159–168.

Aylward, E.H., Augustine, A., Li, Q., Barta, P.E., Pearlson, G.D., 1997. Measurement of frontal lobe volume on magnetic resonance imaging scans. Psychiatry Research: Neuroimaging 75, 23–30.

Castellanos, F., Giedd, J., Marsh, W., Hamburger, S., Vaituzis, A., Dickstein, D., Sarfatti, S., Vauss, Y, Snell, J, Lange, N., 1996. Quantitative brain magnetic resonance imaging in attention deficit hyperactivity disorder. Archives of General Psychiatry 53, 607–616.

Christensen, G.E., Rabbitt, R.D., Miller, M.I., 1994. Three-di-

mensional brain mapping using a deformable neuroanatomy. Physics in Medicine and Biology 39, 609–618.

Collins, D.L., Neelin, P., Peters, T.M., Evans, A.C., 1994. Automatic three-dimensional intersubject registration of MR volumetric data in standardized Talairach space. Journal of Computer Assisted Tomography 18, 192–205.

Gordis, L., 1996. Epidemiology. W.B. Saunders, Philadelphia.

Kaplan, D.M., Liu, A.M.C., Abrams, M.T., Warsofsky, I.S., Kates, W.R., White, C.D., Kaufmann, W.E., Reiss, A.L., 1997. Application of an automated parcellation method to the analysis of pediatric brain volumes. Psychiatry Research: Neuroimaging 76, 15–27.

Ono, M., Kubik, S., Abernathey, C.D., 1990. Atlas of the Cerebral Sulci. Thieme Medical Publishers, Inc. New York.

Otsu, N., 1979. A threshold selection method from gray-level histograms. IEEE Transactions on Systems, Man, and Cybernetics SMC-9, 62–66.

Piven, J., Berthier, M.L., Starkstein, S.E., Nehme, E., Pearlson, G., Folstein, S., 1990. Magnetic resonance imaging evidence for a defect of cerebral cortical development in autism. American Journal of Psychiatry 147, 734–739.

Piven, J., Arndt, S., Bailey, J., Andreasen, N., 1996. Regional brain enlargement in autism: a magnetic resonance imaging study. Journal of the American Academy of Child and Adolescent Psychiatry 35, 530–536.

Rademacher, J., Galaburda, A.M., Kennedy, D.N., Filipek, P.A., Caviness, V.S., Jr., 1992. Human cerebral cortex: localization, parcellation and morphometry with magnetic resonance imaging. Journal of Cognitive Neuroscience 4, 352–374.

Reiss, A.L., Abrams, M.T., Greenlaw, R., Freund, L., Denckla, M.B., 1995. Neurodevelopmental effects of the FMR-1 full mutation in humans. Nature Medicine 1, 159–167.

Reiss, A.L., 1998. BrainImage. Department of Psychiatry, Stanford University, Stanford, CA.

Reiss, A.L., Hennessey, J.G., Rubin, M., Beach, L., Abrams, M.T., Warsofsky, I.S., Liu, A.M.C., Links, J.M., 1998. Reliability and validity of an algorithm for fuzzy tissue segmentation of magnetic resonance images. Journal of Computer Assisted Tomography 22, 471–479.

Subramaniam, B., Naidu, S., Reiss, A.L., 1997a. Neuroanatomy of Rett syndrome: Cerebral cortex and posterior fossa. Neurology 48, 399–407.

Subramaniam, B., Hennessey, J.G., Rubin, M.A., Beach, L.S., Reiss, A.L., 1997b. Software and methods for quantitative imaging in neuroscience: The Kennedy Krieger Institute Human Brain Project. In: Koslow, S.H., Huerta, M.F. (Eds.), Neuroinformatics: An Overview of the Human Brain Project. Lawrence Erlbaum, Mahwah, NJ.

Talairach, J., Tournoux, P., 1988. Co-Planar Stereotaxic Atlas of the Human Brain. Theime Medical Publishers, Inc., New York.

Thorndike, R.L., Hagen, E.P., Sattler, J.M., 1986. The Stanford-Binet Intelligence Scale, 4th ed. The Riverside Publishing Company, Chicago.

Wechsler, D., 1991. Wechsler Intelligence Scale for Children, 3rd ed. The Psychological Corporation, San Antonio, TX.